

# 1 Thermal Performance Analysis of an Underground Closed Chamber with 2 Internal Heat Sources under Natural Convection

3 Zujing Zhang<sup>a,c</sup>, Rodney Day<sup>b</sup>, Kequan Wang<sup>c</sup>, Hongwei Wu<sup>b\*</sup>, Yanping Yuan<sup>a\*\*</sup>

4  
5 <sup>a</sup>School of Mechanical Engineering, Southwest Jiaotong University, Chengdu, 610031, China <sup>b</sup>School of  
6 Engineering and Technology, University of Hertfordshire, Hatfield, AL10 9AB, United Kingdom

7 <sup>c</sup>Chongqing Research Institute of China Coal Technology & Engineering Group, Chongqing, 400037, China

8  
9 \*  
10 Corresponding author. Email: h.wu6@herts.ac.uk. \*\*Corresponding  
11 author. Email: ypyuan@home.swjtu.edu.cn

12  
13 **Abstract** : In this article, a combined experimental and numerical study has been performed to  
14 investigate the thermal performance of mine refuge chamber (MRC) under natural convection. By  
15 using heat lamps to simulate human heat loss, a 20-hour heating experiment is carried out in a fifty-  
16 person MRC laboratory. A proposed numerical model is validated against the experiment.  
17 Furthermore, sensitivity analysis is performed by Fluent software to investigate the effects of thermal  
18 parameters of rock. Results indicated that: (1) the experimental data and the corresponding numerical  
19 prediction have the same trend in air temperature rising with time, and the deviation between the two  
20 is less than 10%, which proves that the numerical model is effective; (2) the temperature rise process  
21 in a MRC can be divided into air temperature rapid increase stage and air temperature slow increase  
22 stage; (3) a new analytical method with simplified for predicting air temperature is proposed, it shows  
23 that the air temperature growth trend becomes slow with the increase of thermal conductivity, density  
24 and specific heat capacity of the rock; (4) the surface heat transfer coefficient of vertical walls is the  
25 largest and it increases linearly with air temperature.

26 **Keywords:** Mine refuge chamber; Coal mine safety; Temperature; Natural convection; Surrounding  
27 rock; Thermal performance.

<b>Nomenclature</b>			
$a$	Thermal diffusivity of rock, $m^2/h$	$a = \lambda/(\rho C_p)$	
$A$	Area, $m^2$		$\Gamma'$ Fluctuating temperature
$b$	Assuming temperature variables, $^{\circ}C$		$\Gamma_0$ Initial rock temperature, $^{\circ}C$
$1$	Turbulence model parameter		$u$ Air velocity, $m/s$
$2$	Turbulence model parameter		$u', u'$ Corresponding fluctuating velocity components
$1\epsilon$	Turbulence model parameter		$x, y$ in the i and j directions
$3\epsilon$	Turbulence model parameter		Coordinate direction vector
$C_a$	Thermal capacity of air, $J/(kg.K)$		<b>Subscripts</b>
$C_b$	Thermal capacity of rock, $J/(kg.K)$		a Air
$F_0$	Fourier Number		c Cross section of the original tunnel
$b$	Generation of turbulence kinetic energy due to buoyancy ( $J/s.m^3$ )		f flow air
$k$	Generation of turbulence kinetic energy due to the mean velocity gradients ( $J/s.m^3$ )		n Numerical simulation
$G$	Grashof number, $G_r = \alpha_v \Delta t l^3 / \nu^2$		i, j Elemental directions (i, j = 1, 2 and 3 corresponding to the x, y, and z directions)
$h$	Natural convective heat transfer coefficient between air and wall, $W/(m^2.K)$		u Unaffected by the external Environment
$h_0$	Initial Natural convective heat transfer coefficient between air and wall, $W/(m^2.K)$		w Walls in a MRC
$k$	Turbulent kinetic energy ( $J/kg$ )		<b>Greek symbols</b>
$k_1$	Gradient for surface heat transfer coefficient		$\chi_v$ Air volume expansion coefficient
$2$	Assuming constants for $K$		
$k$	Gradient for air temperature increasing		
$lK$	Turbulence length scale, $m$		
$m, n$	Assuming constants for $K$		
$N$	Number of people in a MRC		
$P$	Pressure, $Pa$		
$P_r$	Planck number, $P_r = u/a$		
$q$	Heat flux on wall surface, $W/m^2$		
$q_0$	Heat generation rate per person, $W$		
$Q$	Total heat generation rate, $W$		
$r$	Radius of the surrounding rock, $m$		
			$\rho$ Density, $kg/m^3$
			$\lambda$ Thermal conductivity, $W/(m.K)$
			$\mu$ Dynamic viscosity, $kg/m.s$
			$\nu$ Kinematic viscosity, $(kg/m.s)$
			$\nu$ Turbulent eddy viscosity, $(kg/m.s)$
			$\nu$ Turbulence model parameter
			$\nu$ Turbulence model parameter
			<b>Acronyms</b>
			MRC Mine refuge chamber

$r_0$	Equivalent radius of the cylinder, m	PCM	Phase change material
$S$	Modulus of the mean rate-of-strain tensor	UB	Underground building
$T$	Temperature, °C	Re	Reynolds number

## 1. Introduction

With the rapid development and application of underground energy and space, the safety of underground space is becoming an important issue [1]. According to statistics of underground fire and explosion accidents, only a few people among the deaths died directly from the fire and blast wave, and up to 80% of the people indirectly died from carbon monoxide and suffocation [2-5]. The application of underground emergency refuge system, such as the tunnel rescue station in subway, mine refuge chamber (MRC) and movable shelter in mine, plays an important role in reducing deaths for underground accidents [6-8].

MRC is the most important emergency refuge system for underground mine in China, it is also applied in other developed mining countries. A MRC normally consists of a living room and two transition rooms [9], and it needs to serve at least 96 h [10, 11]. Due to the heat generated by human metabolism, the air temperature in the MRC may beyond the allowable range of human's thermal tolerance. The recommended apparent temperature in MRC is below 35 °C [12]. Li et al. [13] concluded that human responses change significantly when exposed in an environment with the temperature of 33 °C or the relative humidity of 85% in MRC. Du et al. [14] recommend that the temperature and relative humidity in MRC should be less than 31 ° and 80% RH. It needs to be mentioned here that the conventional refrigeration technology can't be applied in MRC, because the power may be interrupted after an accident. Therefore, it is imperative to seek new cooling methods for MRC. Jia et al. [15] proposed a temperature control strategy by using ice storage capsule for movable MRC. The accuracy of the strategy was verified by a 24-h experiment in a closed cabin. Wang et al. [16] developed an ice thermal storage system, the system was determined in a fifty-person MRC for approximately 64.57 h. Xu et al. [17] proposed a non-electric cooling scheme for placing the encapsulated ice plates directly in the MRC, one plate has an average cooling load of 14.3 W. Yang et al. [7] designed an open cycle carbon dioxide refrigerator system. A test showed that the system had 1200 W cooling power. Yuan et al. [18] proposed a coupled cooling method and application of phase change material (PCM) combined with pre-cooling of the envelope for MRC, the method considered the applicable temperature range of PCM and the cold storage function of the rock. Gao et al. [19, 20, 21] studied the temperature controlling characteristics of PCM plates and PCM seats used in a fifty-person MRC, the coupled heat transfer characteristics of surrounding rock, air and PCM were considered in their model.

The heat transfer between the heat source, air and surrounding rock in MRC is a dynamic coupling process, thus the calculation of heat transfer is very complex. In recent years, some studies on coupling heat transfer characteristics of air and surrounding rock in the underground building (UB) have been reported. Yuan et al. [22, 23] established a mathematical heat transfer model for underground engineering envelope, the model provided a rapid and accurate solution for calculation of heat transfer. Their results indicated the thermal conductivity of the rock is an important factor of the heat transfer. Xiao et al. [24] proposed a method to calculate the transient heat flow through the envelope of an underground cavern and proved that the method has a good agreement with the numerical results. Liu et al. [25] presented a numerical model for the simultaneous heat transfer between air and the tunnel surface. The model was validated against experimental data applied to an underground tunnel. Kajtar et al. [26] presented a dimensioning method for shallow buried UB in terms of heat transfer characteristics and thermal comfort. The method was in favor of the quick sizing of the required heating and cooling performance of UB. Szabó et al. [27] developed a new dynamic dimensioning method for shallow buried UB. According to the method, there is no significant change in air and wall temperature after 1000 h, as well as the heat flux through the wall.

Sasmito et al. [28] studied the thermal management strategies of a dead end ventilated through a pipe in an underground mine, their results showed that several control parameters, such as virgin rock temperature, ventilation temperature and ventilation amount, have a significant effect on air temperature control. Habibi et al. [29] built a ventilation model calibrated against pressure, quantity and temperature results to simulate the airflow and heat conditions for a coal mine. For both flow and temperature, the predicted results agreed to within 90% accuracy of the actual measurements. Li et al. [30] pointed out that relative roughness plays an important role in the heat transfer of underground tunnels. As the relative roughness increase, the temperature drop and the cooling efficiency increase gradually.

In summary, for the temperature control in MRC, the development of non-powered refrigeration technology has attracted much attention, few studies have focused on the thermal performance of the MRC. In this article, the characteristics of the dynamic coupling heat transfer process between the surrounding rock and the air in a heated MRC are mainly studied. A fifty-person MRC is selected as a study case. A heating experiment is carried out in a MRC laboratory to present the air temperature rising trend. Then ten cases with different parameters are designed to investigate the thermal performance of MRC under natural convection by using Fluent 18.0 software.

## 2. Experimental setup

### 2.1. Experimental environment

A MRC is usually located in a deep underground coal mine. Due to the safety needs of the coal mine and the lack of mineral intrinsic safety heating equipment in the market, the heating experiment is conducted in a shallow MRC laboratory. The laboratory can accommodate 50 people in the living room with 20 m in length, 4 m in width and 3 m in height. The top of the living room is 0.6 m above the ground. The wall was made of concrete with the density of  $1600 \text{ kg/m}^3$ , the specific heat capacity of  $840 \text{ J/(kg}\cdot\text{K)}$  and the thermal conductivity of  $0.81 \text{ W/(m}\cdot\text{K)}$ . The thickness of the vertical and bottoms wall is 0.6 m, 0.4 m for the top wall. A polyurethane insulation layer is covered on the top wall with a thickness of 0.08 m. The thermal conductivity of polyurethane is  $0.024 \text{ W/(m}\cdot\text{K)}$ . In addition, the MRC laboratory is located in a factory, it can avoid the sun shining on the walls of the MRC laboratory.

The experiment is performed in September, the heating process starts at 8 a.m. The atmospheric temperature ranges at  $22 \sim 26 \text{ }^\circ\text{C}$  during the day (from 8 a.m. to 7 p.m.) and  $18 \sim 22 \text{ }^\circ\text{C}$  in the night.

### 2.2. Measurement and data acquisition

When a man sitting quietly in the MRC, the heating rate can be assumed to be 120 W and the rate of  $\text{CO}_2$  released is  $0.30\sim 0.35 \text{ ml/min}$  [9, 31, 32]. Some measures need to be taken to remove the  $\text{CO}_2$  gas. When calcium hydroxide is used to remove  $\text{CO}_2$ , the heat load is 20-25 W per person. But the heat load may not be released into MRC through a reasonable design of purification equipment. If  $\text{CO}_2$  is removed by fresh air, there will be no heat generated. Therefore, the heat generated by facilities in MRC is not considered in our study.

In the experiment, 40 heat lamps with 150 W, representing the heat production of 50 persons, are divided into 4 rows $\times$ 10 columns. The row spacing is 1 m and the column spacing is 1.2 m. All heat lamps are 1 m above the bottom as illustrated in Fig. 1. Six measuring points are respectively set at the three horizontal levels of 0.5 m, 1 m, and 1.5 m. The distance from these measuring points to the near side wall is 1 m. The location of the measuring points can be seen in Fig. 1.

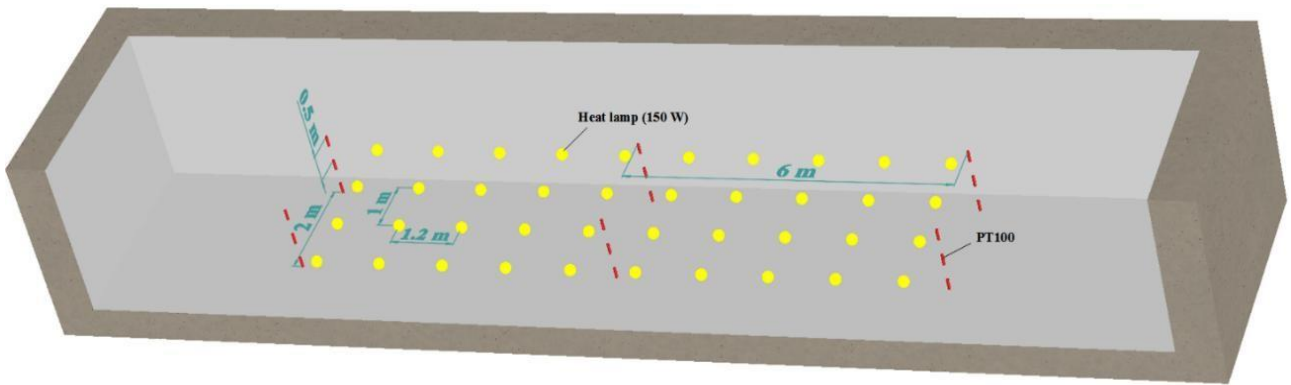


Fig. 1. Distribution of heat lamps and temperature sensors.

The calibrated PT100 (model: WZP-PT100 A; manufacturer: Hangzhou Meacon automation technology Co., Ltd, China) with a measuring range of  $-50 \sim 250 \text{ }^{\circ}\text{C}$  and accuracy of  $0.15 \text{ }^{\circ}\text{C}$  is chosen to measure the air temperature. And a calibrated infrared thermal imager (model: CEM DT-9868; manufacturer: Shenzhen CEM Co., Ltd, China) with a display accuracy of  $0.1 \text{ }^{\circ}\text{C}$  is used to test the initial temperature of the surrounding rock wall surface. The air temperature is collected by a data acquisition subsystem, then transmitted to a temperature monitoring platform and automatically recorded once per minute. The power stability of the heating lamps is guaranteed by a stable voltage power control cabinet. The working condition of the heating lamps and the air temperature measurement system can be controlled in an independent control room. Fig. 2 shows the schematic of the experimental apparatus.

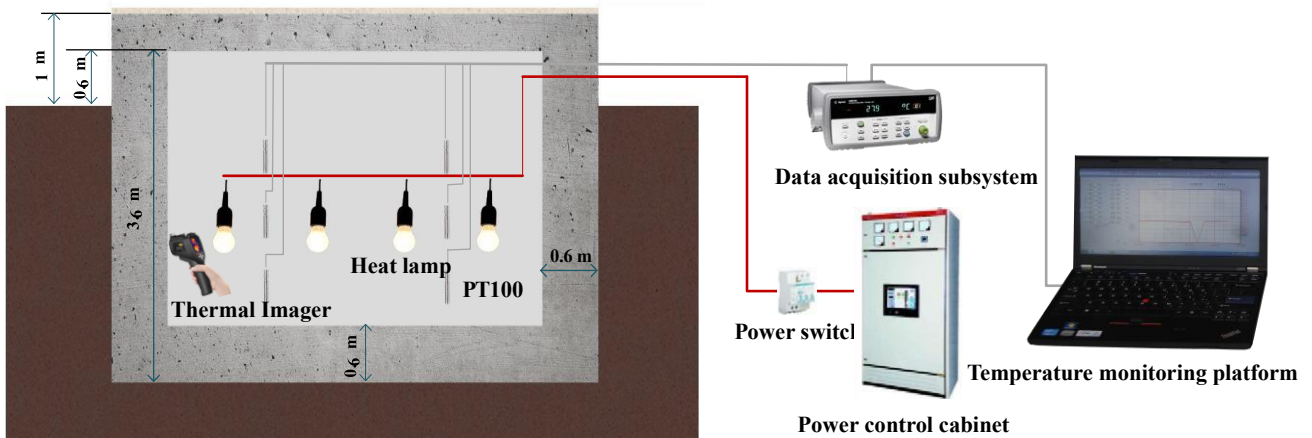


Fig. 2. Schematic of the experimental apparatus.

### 2.3. Experimental procedure

The key steps of the experiment are as follows:

- (1) Check to make sure that all heating lamps and all temperature sensors can work properly and the data can be automatically recorded.
- (2) Prior to heating, measure five points on each wall, the average temperature of all measuring points is taken as the initial temperature of the wall. The value is  $22.3 \text{ }^{\circ}\text{C}$ . After the measurement, the tester leaves the lab and closes the laboratory's door.

(3) Prior to heating, turn on the temperature monitoring platform half an hour before heating to test the initial air temperature, the average air temperature is taken as the initial air temperature in the MRC laboratory. The value is 25 °C.

(4) Turn on the heating lamps in the control room, heating lasts more than 20 h.

(5) End the experiment and save the experimental data. Fig. 3 shows the actual heating scene in



the experiment.

**Fig. 3. Normal operation of the heating experiment.**

### 3. Computational details

#### 3.1. Analytical model

The buried depth of an underground mine is usually greater than 100 m. According to [33], the heat transfer characteristics of underground buildings with a buried depth greater than 12 m are not affected by the ground environment temperature. The thermal performance of deep buried underground buildings can be analyzed based on the semi-infinite object heat transfer theory. The controlling equations can be established in the one-dimensional coordinate system. The equation for calculating the changes in the temperature of MRC is:

$$\frac{\partial T(x, \tau)}{\partial \tau} = a \frac{\partial^2 T(x, \tau)}{\partial x^2} \quad (1)$$

Boundary conditions can be described as

$$\begin{cases} \lambda \frac{\partial T(x, \tau)}{\partial x} \Big|_{x=0} = h (T_f(\tau) - T(x, \tau)) \\ \lim_{x \rightarrow \infty} \frac{\partial T(x, \tau)}{\partial x} = 0 \end{cases} \quad (2)$$

Initial condition can be described as

$$T(x, 0) = T_0 \quad (3)$$

In order to simplify the heat transfer process in a heated MRC under the natural convection, several assumptions could be made as follows:

- (1) The shape of the MRC is cylindrical. Huang et al. [33] proved that the temperature contour in the rock formation is approximately circular for different shape tunnels. The equivalent radius of the cylinder can be calculated as  $r_0 = \sqrt{A_c/\pi}$ ;
- (2) The heat production rate of each person is equal and constant because people in MRC are basically quiet;
- (3) The heat absorbed by air can be ignored because the specific heat capacity of air is much smaller than that of rock;
- (4) Heat transfer on the wall surfaces is uniform and can be regarded as a constant because the thermal parameters of the surrounding rock are uniform;
- (5) The temperature inner the surrounding rock is equal everywhere at the initial time because the heat transfer characteristics of MRC is not affected by the environment temperature.

Therefore, in the cylindrical coordinate system, the governing equation of heat conduction can be described as follows

$$\frac{\partial T(r, \tau)}{\partial \tau} = a \left( \frac{\partial^2 T(r, \tau)}{\partial r^2} + \frac{1}{r} \frac{\partial T(r, \tau)}{\partial r} \right) \quad (4)$$

The boundary conditions can be described as

$$\begin{cases} \lambda \frac{\partial T(r, \tau)}{\partial r} \Big|_{r=r_0} = q = \frac{Q}{A_w} = \frac{N \cdot q_0}{A_w} = const \\ \lim_{r \rightarrow \infty} T(r, \tau) = T_0 \end{cases} \quad (5)$$

The initial condition is

$$T(r, 0) = T_0 \quad (6) \text{ An approximate}$$

solution regarding the temperature of the wall surface was recommended as [33]

$$T(r_0, \tau) = t_0 + \frac{q \cdot r_0}{\lambda} \frac{1.13 \sqrt{F_0}}{1 + 0.38 \sqrt{F_0}} \quad (F_0 = a \cdot \tau / r_0^2) \quad (7)$$

According to Newton's law of cooling



$$q = h[T_f(\tau) - T(r_0, \tau)] \quad (8)$$

Thus, the air temperature in a MRC can be calculated as

$$T_f(\tau) = T_0 + q \left( \frac{1}{h} + \frac{r_0}{\lambda} \frac{1.13\sqrt{F_0}}{1+0.38\sqrt{F_0}} \right) \quad (9)$$

The natural convective heat transfer coefficient between the air and wall can be calculated as [21]

$$h = \frac{\lambda_a \cdot Nu}{l} = \frac{\lambda_a}{l} \times 0.59 \times (G_r \cdot P_r)^{\frac{1}{4}} \quad (10)$$

The air temperature increase value in the MRC was then computed by

$$\Delta T_f(\tau) = T_f(\tau) - T_0 = q \left( \frac{1}{h} + \frac{r_0}{\lambda} \frac{1.13\sqrt{F_0}}{1+0.38\sqrt{F_0}} \right) \quad (11)$$

The radius of the heat transfer zone of the rock can be calculated as [34]

$$r = 4\sqrt{a \cdot \tau} \quad (12) \text{ According to the}$$

Eq. (9), it can be seen that the final air temperature in a MRC has a direct relationship with the rock initial temperature. However, according to the Eq. (11), the air temperature increasing value in MRC has nothing to do with the initial rock temperature, it's just affected by the thermal parameters of the rock and the heat load on the walls. It is obvious that the increased value is linearly proportional to the heat load on the walls. The heat load is mainly determined by the power of heat sources and the total surface area of the walls, which has nothing to do with the shape and size of the heat sources (miners in the MRC). In addition, as the buried depth of a MRC is much larger than 12 m, the depth will no longer affect the heat transfer characteristics of the MRC. Therefore, in the following numerical study, the burial depth of MRC, the initial rock temperature, the human heat loss, as well as the shape and size of human bodies will not be considered as the main influencing factors. And the effects of the thermal conductivity and the specific heat capacity, as well as the density of the rock on heat transfer characteristics will be emphasized.

### 3.2. Computational model

A computational model of MRC is built with the same inner sizes of the MRC laboratory (length  $\times$  width  $\times$  height: 20 $\times$ 3 $\times$ 4 m). The thickness of the wall is 1.5 m. The surface area of a human body model is 2 m<sup>2</sup>. 50 bodies are divided into 4 rows, as shown in Fig. 4. For the two rows adjacent to the two sides of the room, each row has 13 bodies, the back of the body is 0.3 m from the wall. For the two rows in the middle, each row has 12 bodies, The distance between two bodies' backs is 0.4 m. The center distance between the two adjacent bodies in a row is 1 m. Meanwhile, in order to obtain a high-quality boundary layer grid, the bottom surface of human body is above the bottom 0.35 m.

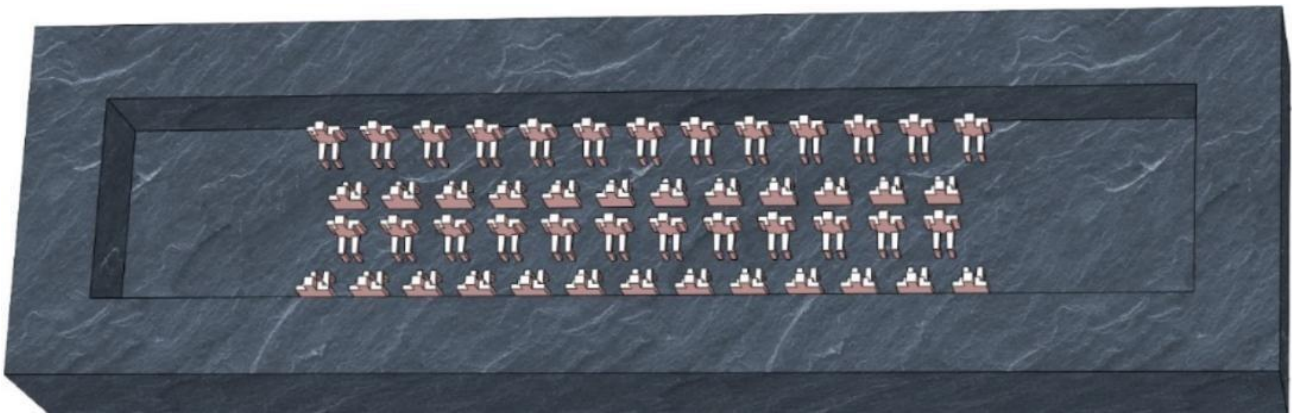


Fig. 4. Geometric model of the fifty-person MRC.

The computational grids are generated by software ANSYS ICEM 18.0. Six grids (with a number of grids as  $10.2 \times 10^5$ ,  $13.8 \times 10^5$ ,  $17.6 \times 10^5$ ,  $27.5 \times 10^5$ ,  $35.0 \times 10^5$ ,  $41.4 \times 10^5$ , respectively) are tested to ensure that the solver and numerical schemes implementation yield results are independent from the grid, as shown in Fig. 5.

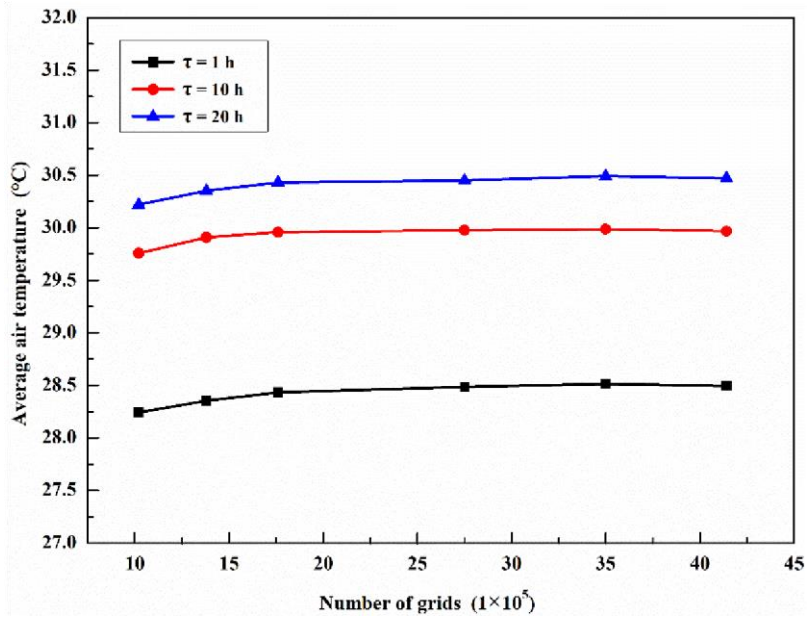


Fig. 5. Comparison of air temperature at three different time under six different grids.

It has been concluded that the mesh with  $17.6 \times 10^5$  grids is sufficient. The maximum grid size of the inner wall surface is 0.1 m. In the fluid zone. 4 prism layers are created along the surrounding. The maximum grid size of human body surfaces is 0.06 m. The maximum grid size of the fluid zone and the solid zone is 0.3 m and 0.5 m, respectively.

### 3.3. Numerical methodology

Human bodies are defined as solid zones with a constant temperature of  $37^\circ$ . Shadow surfaces will be generated automatically at the surfaces of human bodies in the Fluent software. The surfaces of the human bodies adjacent to the fluid zone are defined as constant heat flux boundary with  $60 \text{ W/m}^2$ , and the shadow surfaces adjacent to the human body solid zones are defined as heat flux boundary with  $0 \text{ W/m}^2$ . The inner walls of the surrounding rock are defined as the coupled boundary.

The outer walls of the surrounding rock are defined as heat flux boundary with  $0 \text{ W/m}^2$ .

In combination with the thermal parameters of the surrounding rock of the MRC laboratory and the thermal parameters of common rocks in mine, ten different cases are designed, see Table. 1.

NO	$^\circ\text{C}$ $\text{W}/(\text{m}\cdot\text{K})$	$^\circ\text{C}$	$\rho$ $\text{kg}/\text{m}^3$	$C_p$	$\tau_u$	$\tau_n$
					$\text{J}/(\text{kg}\cdot\text{K})$	
					<b>h</b>	<b>h</b>

**Table. 1 Thermal physical parameters for the ten numerical cases**

The parameters in the NO.1 case correspond to the experiment. The remaining cases are designed

1	25	22.3	0.81	1600	840	64.81	60
2	20	20	1	2400	920	86.25	60
3	20	20	1.50	2400	920	57.50	20
4	20	20	2	2400	920	43.12	20
5	20	20	2.50	2400	920	34.50	20
6	20	20	3	2400	920	28.75	20
7	20	20	2	2400	800	37.5	20
8	20	20	2	2400	1100	51.56	20
9	20	20	2	2000	920	35.93	20
10	20	20	2	1500	920	26.95	20

to investigate the effects of thermal parameters of the rock, the initial temperature of the air and the rock are set as 20 °C. According to Eq. (12), the time that the heat transfer characteristics of the MRC model unaffected by the external environment for each case is different, the unaffected time ( $\tau_u$ ) for each case is shown in Table. 2. The numerical simulation time ( $\tau_n$ ) for NO.1 and NO.2 is 60 h, for the remaining cases,  $\tau_n$  is 20 h.

### 3.4. Turbulence model

The airflow velocity near the walls in the MRC induced by buoyancy is estimated as 0.02 ~ 0.3 m/s, the Reynolds number (Re) is calculated as  $0.22 \times 10^5 \sim 1.08 \times 10^5$ . Therefore, the air flow in the MRC is considered to be turbulent.

The effects of turbulence are modeled frequently by using the three models of Standard  $k-\varepsilon$ , RNG  $k-\varepsilon$  and Realizable  $k-\varepsilon$  [35]. Wu et al. [36] proved that, for conjugate turbulent natural convection in a differentially heated cavity, the three models were acceptable in terms of the performance of predicting the time-averaged quantities, and the variation between them was very small. Franke et al. [37] indicated that realizable  $k-\varepsilon$  turbulence model had a general good performance for wind flow around buildings. Sørensen et al. [38] indicated that the Realizable  $k-\varepsilon$  had an overall good performance for indoor air flow. Through a study of the natural convection phenomena inside a wall solar chimney, Bacharoudis et al. [39] proved that the realizable  $k-\varepsilon$  model was likely to provide superior performance for flows boundary layers under strong adverse pressure gradients. Piña-Ortiz et al. [40, 41] proved that the Realizable  $k-\varepsilon$  model was the best model for natural convection in a cubic cavity with the lowest temperature difference. Therefore, the Realizable  $k-\varepsilon$  model is selected for the current study.

The buoyancy-induced turbulent air flow within the MRC is governed by the following unsteady Reynolds Averaged Navier–Stokes equations [36]:

The continuity equation is

$$\frac{\partial \rho_a}{\partial \tau} + \frac{\partial(\rho_a u_i)}{\partial x_i} = 0 \quad (13)$$

The momentum equation is

$$\frac{\partial u_i}{\partial \tau} + \frac{\partial(u_i u_j)}{\partial x_j} = -\frac{1}{\rho_a} \frac{\partial p}{\partial x_i} + \frac{1}{\rho_a} \frac{\partial}{\partial x_j} \left[ \mu \left( \frac{\partial u_i}{\partial x_j} + \frac{\partial u_j}{\partial x_i} \right) - \rho_a \overline{u'_i u'_j} \right] - g_i \beta (T - T_0) \quad (14)$$

The Boussinesq approach is applied for the effect of gravity force, the energy equation with Boussinesq assumption is

$$\frac{\partial T}{\partial \tau} + \frac{\partial(u_j T)}{\partial x_j} = \frac{1}{\rho_a} \frac{\partial}{\partial x_j} \left[ \mu \left( \frac{\partial u_i}{\partial x_j} + \frac{\partial u_j}{\partial x_i} \right) - \rho_a \overline{u'_i T'} \right] \quad (15)$$

The realizable k- $\epsilon$  model consists of the following two transport equations[42]:

$$\frac{\partial}{\partial \tau} (\rho_a k) + \frac{\partial(\rho_a k u_j)}{\partial x_j} = \frac{\partial}{\partial x_j} \left[ \left( \mu + \frac{\mu_\tau}{\sigma_k} \right) \frac{\partial k}{\partial x_j} \right] + G_k + G_b - \rho_a \epsilon \quad (16)$$

$$\frac{\partial}{\partial \tau} (\rho_a \epsilon) + \frac{\partial(\rho_a \epsilon u_j)}{\partial x_j} = \frac{\partial}{\partial x_j} \left[ \left( \mu + \frac{\mu_\tau}{\sigma_\epsilon} \right) \frac{\partial \epsilon}{\partial x_j} \right] + \rho_a C_1 S \epsilon + \rho_a C_2 \frac{\epsilon^2}{k + \sqrt{v \cdot \epsilon}} - \rho_a C_{1\epsilon} \frac{\epsilon}{k} C_{3\epsilon} G_b \quad (17)$$

### 3.5. other settings

The gravity value is 9.81 m/s<sup>2</sup>. The operating pressure is 102325 Pa. The air operating density is 1.225 kg/m<sup>3</sup>. The enhanced wall treatment with pressure gradient effects and thermal effects are taken into account, as well as the full buoyancy effect. Pressure-implicit with splitting of operators (PISO) is used for the pressure-velocity coupling. The pressure is discretized by using the body force weighted schemes. The energy and momentum are discretized by using the second-order upwind schemes. The convergence absolute criteria for energy is set to 10<sup>-6</sup>, for other items is 10<sup>-3</sup>. The time step is 10 s.

## 4. Results and discussion

### 4.1. Model validation

Fig. 6 plots the variation of average air temperature with heating time at three different levels, i.e. 0.5 m, 1 m, 1.5 m.

It is observed from Fig. 6 that the average air temperature at the three levels has the same growth trend, the air temperature monotonically increases over time. However, there are slight differences in temperature at different height levels, indicating that the temperature increases with the height. During the period from 2 to 10 h, the air temperature at 1 m level is 0.3~0.4 °C higher than that at 0.5 m level, but 0.2~0.4 °C lower than that at 1.5 m level.

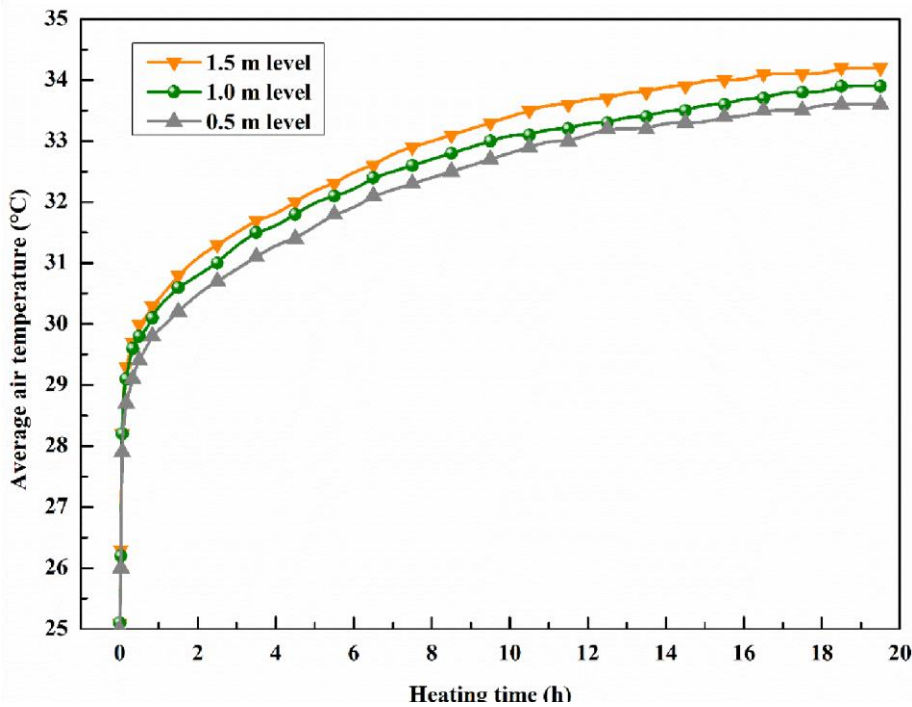


Fig. 6. Variation of air temperature at three different levels, i.e. 0.5 m, 1 m, 1.5 m, with heating time

Fig. 7 shows the comparison of average air temperature between the experimental data and the 302 numerical results of NO.1 case.  
303

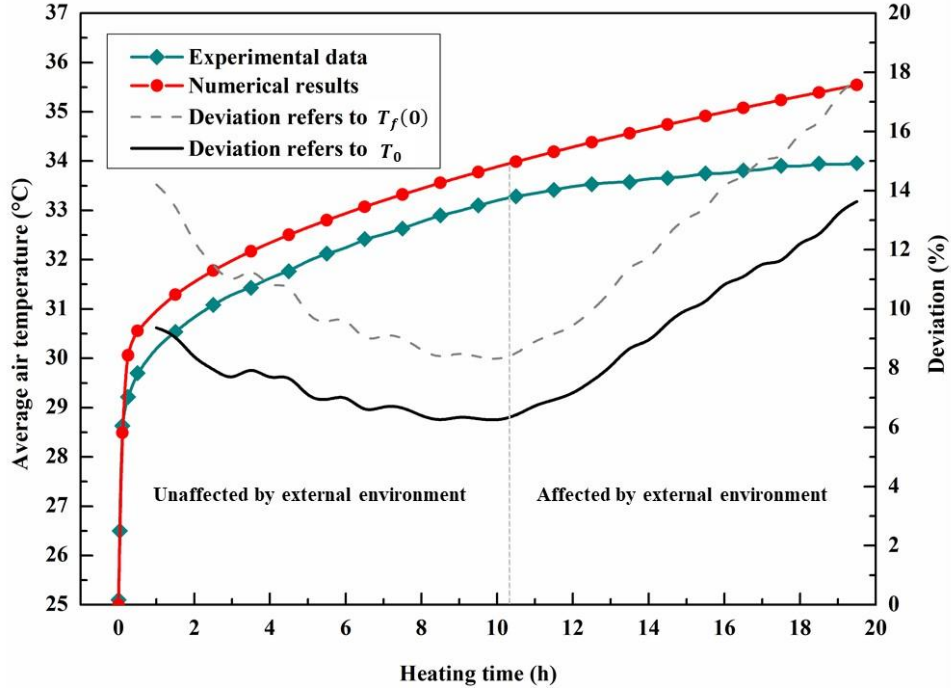


Fig. 7. Comparison of numerical results and experimental data.

It can be seen from Fig. 7 that the average air temperature obtained through the experiment and numerical method has the same trend of rising monotonically with time. In the experiment, the average air temperature in the MRC rises from 25 °C to about 29.5 °C in less than 0.5 h after the heating lamps work. Afterward, the rising trend gradually becomes slow over time. It can be found that the predicted air temperature is higher than the experimental one.

According to Eq. (12), the  $\tau_u$  value is 10.37 h. From 0.5 h to 10.3 h, the average air temperature difference between the experimental value and the predicted value is 0.6~0.8 °C. The temperature deviation between the experimental temperature and the predicted temperature ranges from 8.5% to 14.5%, referencing to the initial air temperature (25 °C) in the MRC. When taking the initial surrounding rock temperature (22.3 °C) as the reference, the deviation value is 6.3%~9.5%. The temperature difference is mainly attributed to two aspects: firstly, the location of the measuring points is relatively low, the measuring value may be smaller than the actual value; secondly, the MRC laboratory experienced a period of time prior to heating, the internal temperature of the rock may not be uniform. From 10.3 h to 20 h, the air temperature rising trend in the experiment becomes slower, and the temperature difference and the deviation both increase with the heating time. It could be explained by the fact that after about 10 h of heating, the experiment began to be affected by the external environment.

At the beginning of the heating, since the experimental result shows that the air temperature is very sensitive and the initial air temperature is higher than the rock temperature, it is not appropriate to take the initial air temperature as the reference. According to Eq. (9), the rock initial temperature is a reasonable reference. So during the unaffected time of the MRC laboratory, the deviation value is less than 10%. On the other hand, it can be easily found that both the numerical results and the

experimental data have an obviously similar trend in air temperature increases. Therefore, it can be concluded that the numerical model is effective.

#### 4.2. Air temperature distribution in the MRC

Fig.8 shows the temperature contours of the center cross-sectional at different time.

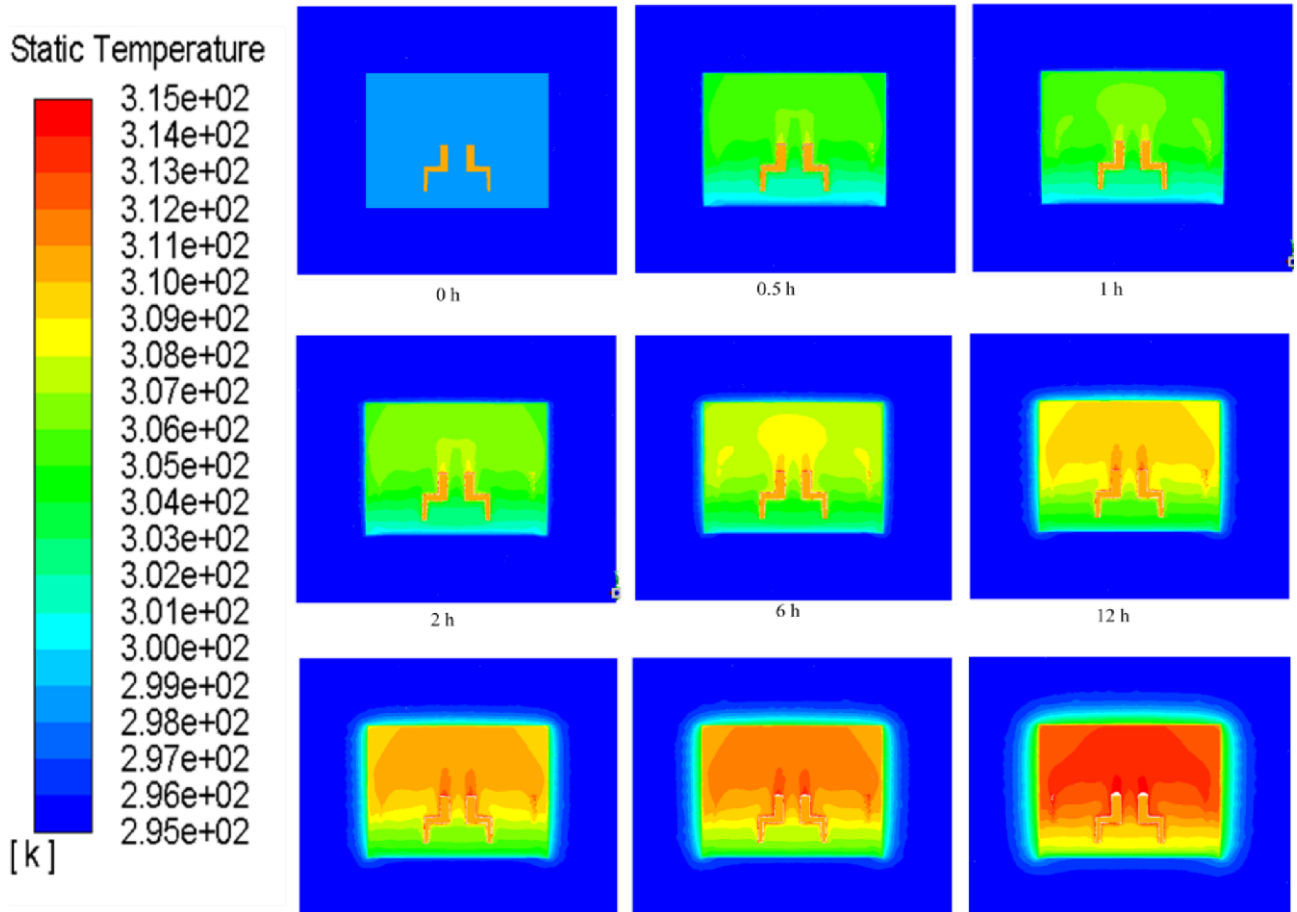


Fig. 8. Contours of temperature distribution at different time.

It can be seen from Fig. 8 that the air temperature in MRC is not uniform. The air temperature above the top surface of the human body is higher than that below the top. In the above part, the air temperature decreases with the height. In the below part, the air temperature increase with the height. The air temperature difference between the top and bottom increases with the heating time.

#### 4.3. Trend of air temperature rising in the heating process

Fig. 9 and Fig. 10 demonstrate the variation of average air temperature with heating time ( $\tau$ ) and the square root of heating time ( $\sqrt{\tau}$ ) in 60 h for NO.1 case, respectively.

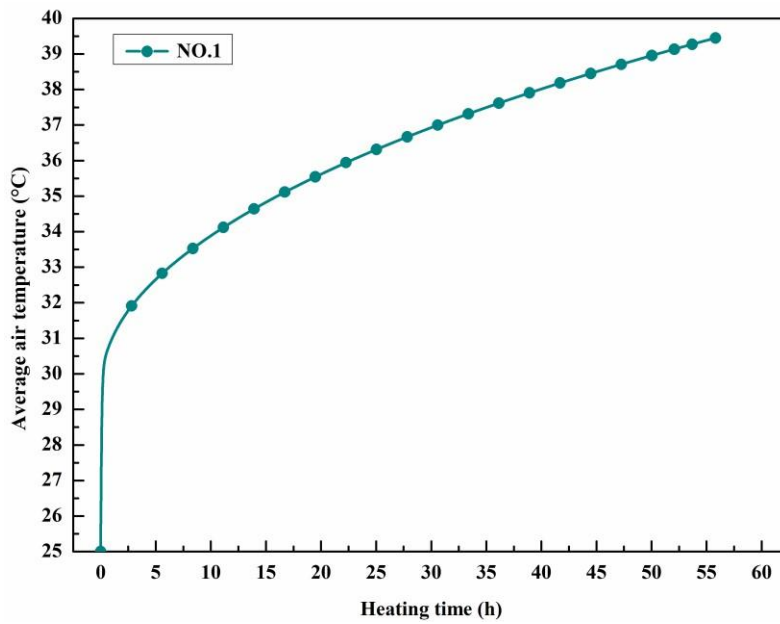


Fig. 9. Air temperature varies with  $\tau$ .

It can be seen from Fig. 9 that the air average temperature in the MRC monotonically increases with time. At the beginning of heating, the air temperature in the room rises quickly, the temperature increasing from 25 °C to 30.2 °C only experiences 0.35 h. Afterward, the increasing rate gradually slows down, the air temperature rising to 35 °C takes about 20 h.

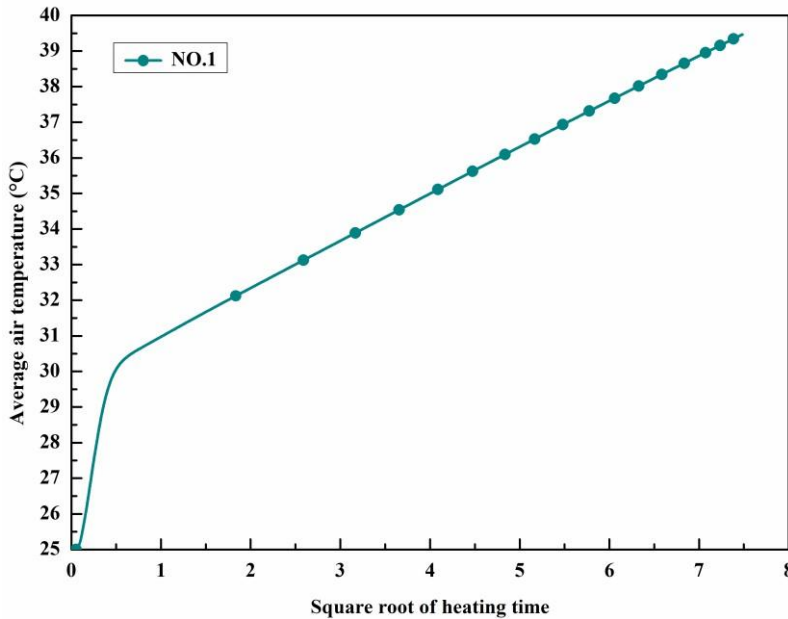


Fig. 10. Air temperature varies with  $\sqrt{\tau}$ .

It can be seen from Fig. 10 that the air temperature rising trend approximately exhibits two linear growth stages. The gradient of air temperature rising in  $\sqrt{\tau} < 0.5$  h is obviously larger than that in  $\sqrt{\tau} > 0.5$  h. Therefore, the process of the air temperature rising in the heated MRC can be divided into two stages, they are air temperature rapid increase stage and air temperature slow increase stage.

During the air temperature rapid increase stage, assume that the air temperature is evenly distributed, according to the principle of energy conservation, there is

360  $Qd\tau = mC_a dT_f(\tau) + hA_w [T_f(\tau) - T(r_0, \tau)]d\tau$  (18) The time of the air temperature rapid increase stage is short (less than 0.5 h), during this time, the temperature of the rock surface changes less. Therefore, it can be assumed that the temperature of the walls does not change. If the initial air temperature is equal to the initial rock temperature, that is

$$T(r_0, 0) = T_f(0) = T_0 \quad (19) \text{ The Eq. (18) can be solved as}$$

$$T_f(\tau) = \frac{q}{h} \left( 1 - e^{-\frac{hA_w}{m \cdot C_a} \tau} \right) + T_0 \quad (20)$$

During the air temperature slow increase stage, it can be easily found from Fig. 10 that the air temperature is obviously linearly related to the square root of heating time, that is

$$T_f(\tau) = K\sqrt{\tau} + b = q \times f(\lambda, \rho, C_p) \sqrt{\tau} + \frac{q}{h} + T_0 \quad (21)$$

#### 4.4. Convective heat transfer coefficient on wall of enclosure structure

Fig. 11 shows the surface heat transfer coefficient of the bottom, the top, as well as the vertical walls changes with the average air temperature in the MRC.

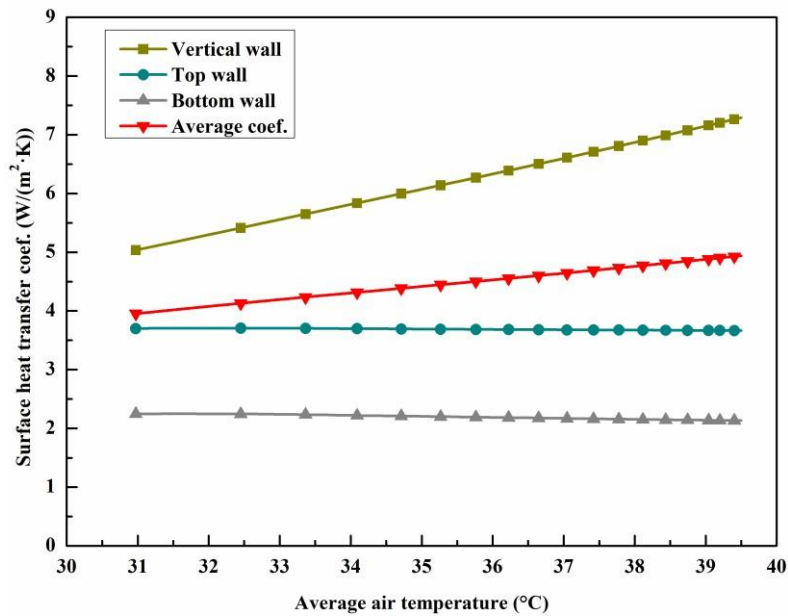


Fig. 11. Wall convective heat transfer coefficient varies with temperature.

It can be seen from Fig. 11 that the surface heat transfer coefficient value in different directions are not equal. The value on the vertical wall is the largest and on the bottom is the smallest. The value of the vertical wall increase monotonically linearly with air temperature, but for the bottom and the top wall, it does not change substantially. It means that, for MRC with same space volume, the trend of air temperature rising can be slowed down by increasing the surface area of the vertical walls. The predicted average natural convection heat transfer coefficient is 3.9~4.8 W/m²·K in the 31~39 °C environment. Yoon et al. [43] found that the average natural convection heat transfer coefficient is 4.53 W/m²·K, by performing a test in an underground tunnel on a summer day with atmospheric temperature range from 23.84 °C to 29.47 °C. But in their test, the sampling points are located on the both-side vertical walls, and the effect of the wall roughness on the value is not well estimated. To some extent, the predicted value is close to the test one.

For the average surface heat transfer coefficient of the MRC, the value shows a linear increase with the air temperature, that is



$$h(\tau) = k_1 [T_f(\tau) - T_f(0)] + h_0 \quad (22)$$

The difference in the convection heat transfer coefficient is mainly due to the uneven distribution of air velocity in the MRC. Fig.12 shows the air velocity magnitude distribution in the MRC at 40 h.

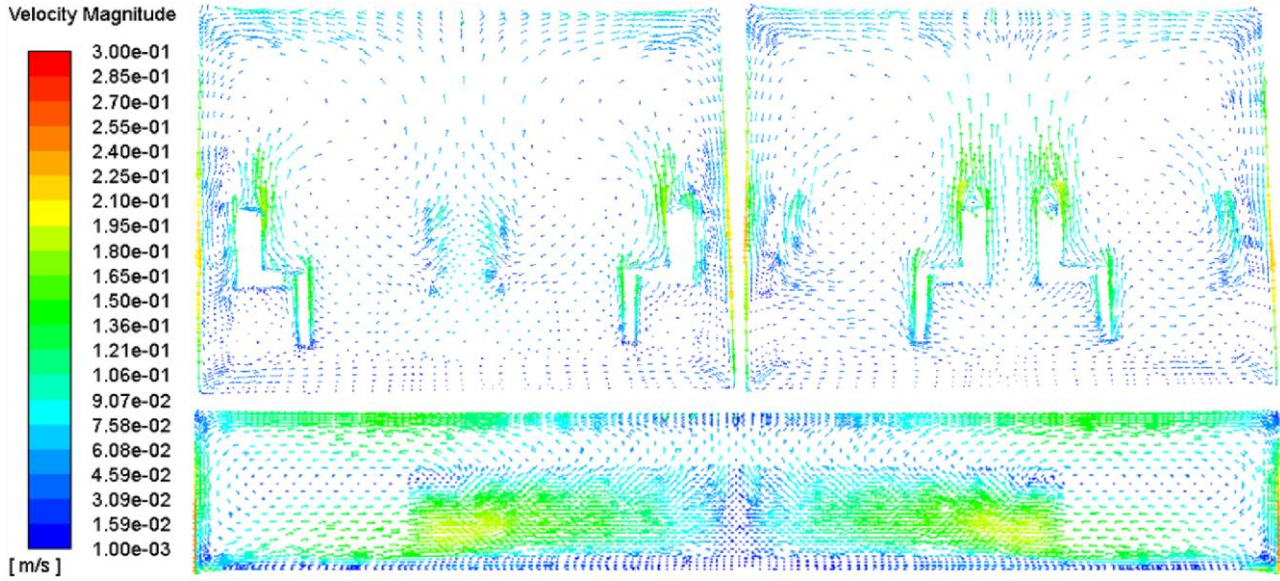


Fig. 12. Air velocity magnitude distribution in the room.

According to Fig. 12, as far as the air velocity direction is concerned, the air moves upward around the heat source bodies, moves horizontally both near the top surface and the bottom surface, moves downward along the vertical wall surfaces. Regarding the air velocity magnitude, the wind speed near the vertical wall is the largest, near the bottom wall is smallest. The maximum wind speed near the vertical wall is 0.25 m/s, 0.12 m/s near the top, and 0.02 m/s near the bottom.

#### 4.5. Effect of thermal parameters of surrounding rock

Fig. 13 plots the air temperature increase with time for the nine different cases NO.2~NO.10.

It can be seen from Fig. 13 that the air temperature monotonically increases with time. At the initial stage of the heating, the air temperature rapidly rises to 27.8~28.3 °C from 20 °C in less than 0.5 h, the curves of the air temperature basically coincide in the nine different cases, it indicates that, during the air temperature rapid increase stage, the  $\lambda$ ,  $\rho$  and  $C_P$  of surrounding rock have no obvious effect on the air temperature rise, which is in good agreement with Eq. (20). When the heating time  $\tau > 0.5$  h, the air temperature rising trend with time gradually becomes slow, and the greater the  $\lambda$ ,  $\rho$  and  $C_P$  of the rock, the slower the air temperature rises. It can be concluded that, during the air temperature slow increasing stage, the air temperature rise rate decreases as the  $\lambda$ ,  $\rho$  and  $C_P$  of the rock increase.

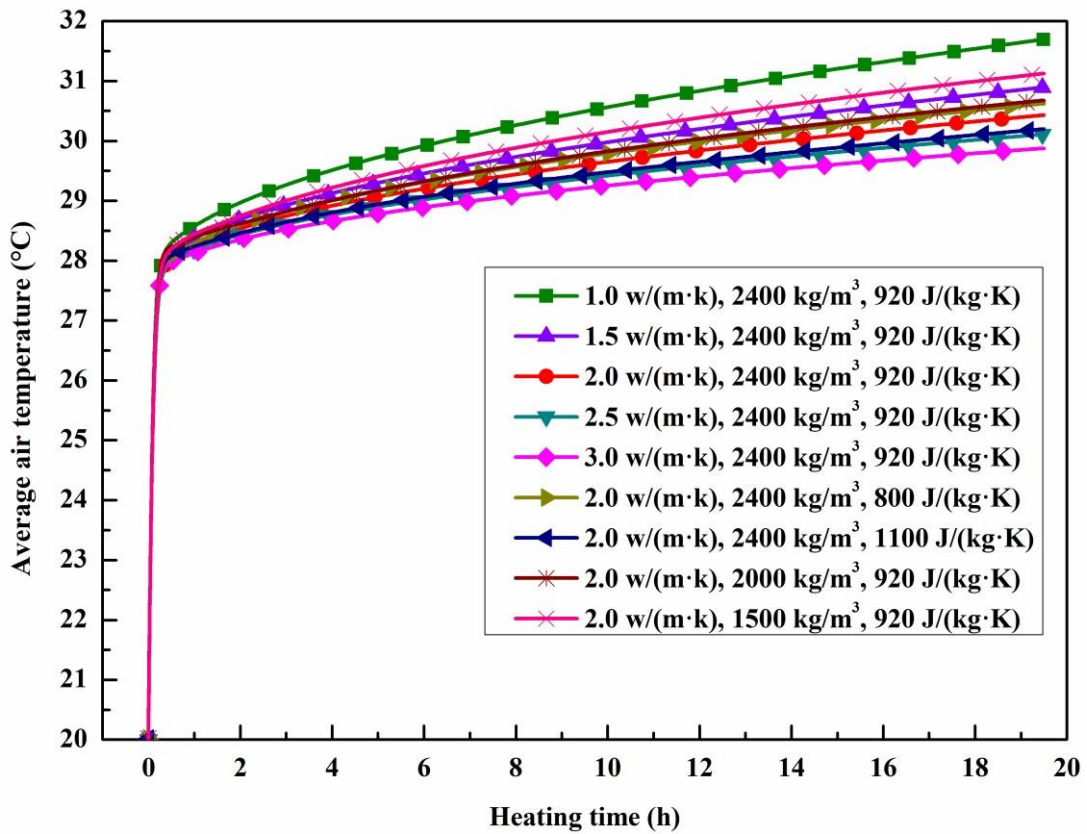


Fig. 13. Air temperature increase with time for different  $\lambda$ ,  $\rho$  and  $C_P$  within 20 h.

Fig. 14 shows the variation of average air temperature with  $\sqrt{\tau}$  at different  $\lambda$ ,  $\rho$  and  $C_P$ .

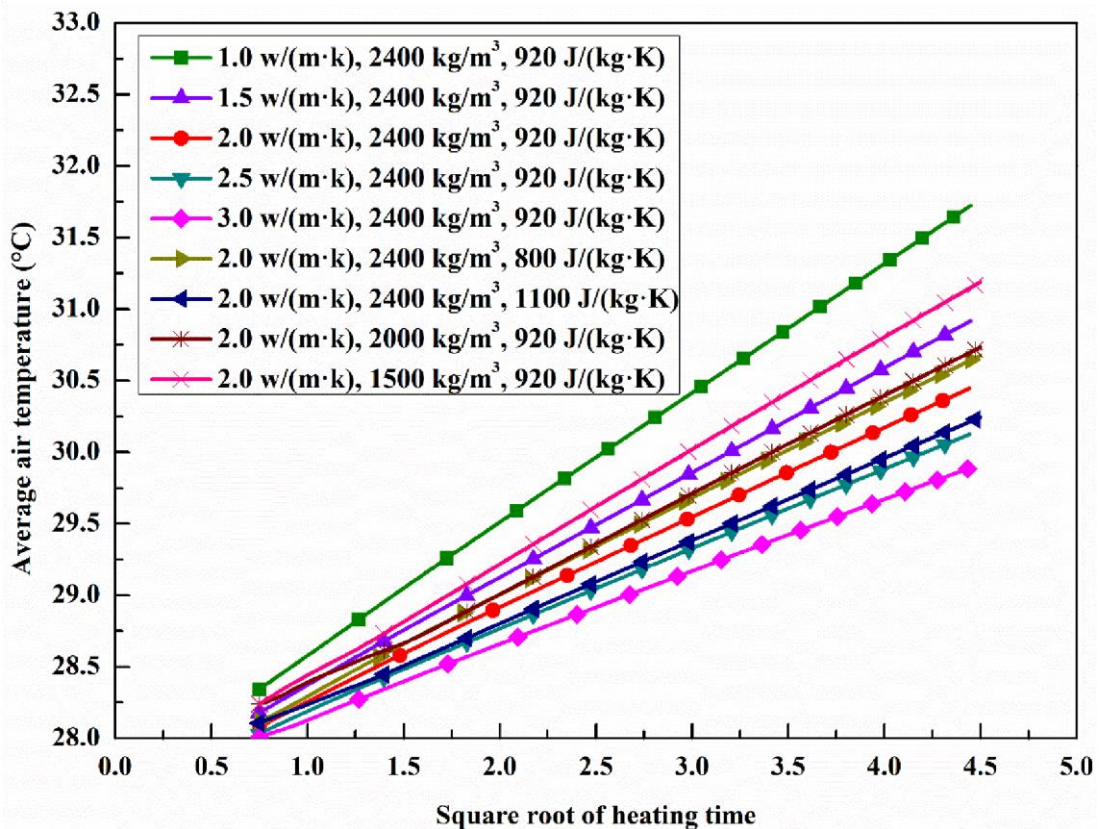


Fig. 14. Variation of average air temperature with  $\sqrt{\tau}$  at different  $\lambda$ ,  $\rho$  and  $C_P$ .

It can be seen from Fig. 14 that, when  $\sqrt{t} > 1.5$  h, the average air temperature increases linearly with  $\sqrt{t}$ . It is not difficult to judge that the value of  $\lambda$ ,  $\rho$  and  $C_P$  mainly influences the linear growth gradient ( $K$ ), the  $K$  value decreases as the  $\lambda$ ,  $\rho$  and  $C_P$  of the rock increase.

#### 4.6. Accurate prediction at the air temperature slow increase stage

(1) Establish the new analytical method

Fitting the original data in Fig. 9 and Fig. 13, the linear fitting formula for different  $\lambda$ ,  $\rho$  and  $C_P$  of the rock is obtained, as shown in Table. 2.

Table. 2 The fitting relation for different  $\lambda$ ,  $C_P$  and  $\rho$  of the rock.

$\lambda$	$\rho$	$C_P$	Linear fitting formula	$K$	$R^2$
W/(m.K)	kg/m <sup>3</sup>	J/(kg.K)			
0.81	1600	840	$y = 1.3014x + 29.772$	1.3014	0.9999
1	2400	920	$y = 0.9082x + 27.688$	0.9082	1
1.5	2400	920	$y = 0.7349x + 27.652$	0.7349	1
2	2400	920	$y = 0.6323x + 27.645$	0.6323	0.9999
2.52400	920	840	$y = 0.5601x + 27.643$	0.5601	0.9999
2	1500	920	$y = 0.7915x + 27.639$	0.7915	0.9999
2	2000	920	$y = 0.6842x + 27.657$	0.6842	0.9996
2	2400	920	$y = 0.6323x + 27.645$	0.6323	0.9999
2	2400	800	$y = 0.6764x + 27.645$	0.6764	0.9998
2	2400	1100	$y = 0.5768x + 27.651$	0.5768	1

Fig. 15 plots the  $K$  value varies with  $1/\sqrt{\lambda}$  (value of  $\rho$  and  $C_P$  are same) and  $1/\sqrt{\rho \cdot C_P} \times 10^3$  ( $\lambda$  value is same), respectively, as well as the corresponding fitting line.

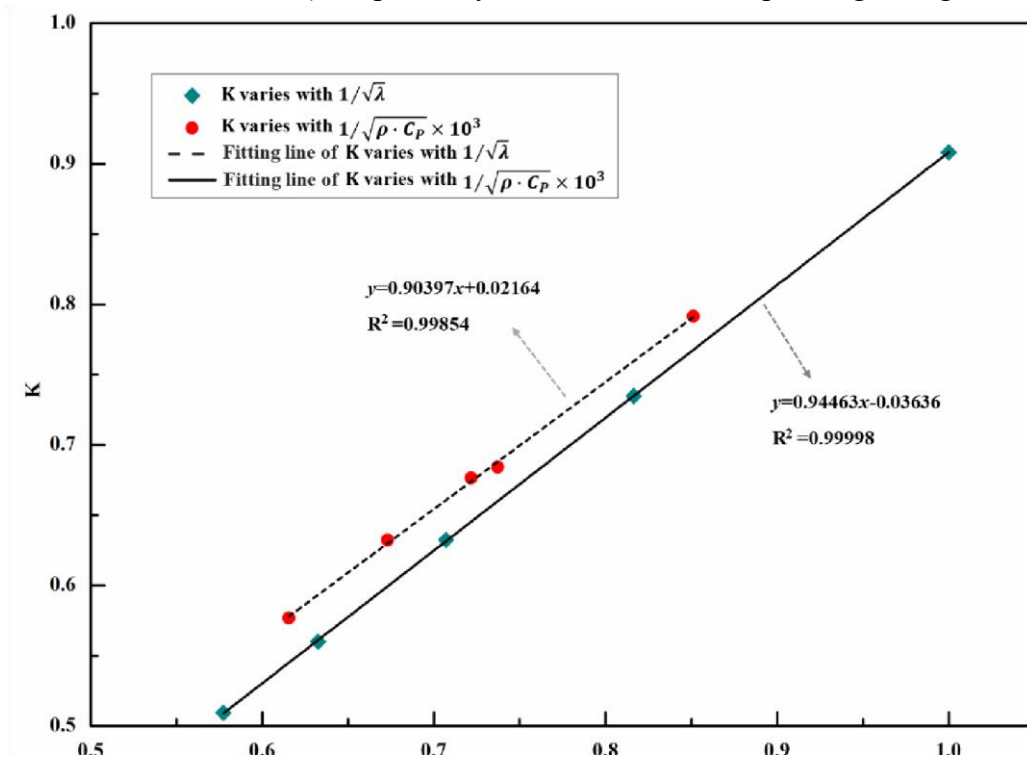


Fig. 15. Gradient  $K$  varies with  $1/\sqrt{\lambda}$  and  $1/\sqrt{\rho \cdot C_P} \times 10^3$

It can be seen from Fig. 15 that the  $K$  value has a linear relationship with  $1/\sqrt{\lambda}$ . Therefore, the Eq. (21) can be further expressed as follow:

$$T_f(\tau) = q \left( \frac{1}{\sqrt{\lambda}} - 0.036 \right) \times f(\rho, C_p) \sqrt{\tau} + \frac{q}{h} + T_0 \quad (23)$$

It can be also seen from Fig. 15 that the  $K$  value has a linear relationship with  $1/\sqrt{\rho \cdot C_p} \times 10^3$ . Therefore, the Eq. (21) can be further expressed as follow:

$$T_f(\tau) = qf(\lambda) \left( \frac{1}{\sqrt{\rho C_p}} \times 10^3 + 0.024 \right) \sqrt{\tau} + \frac{q}{h} + T_0 \quad (24)$$

According to Eq. (23) and Eq. (24),  $K$  can be expressed as:

$$K = qf(\lambda, \rho, C_p) = k_2 \left( \frac{1}{\sqrt{\lambda}} + m \right) \left( \frac{1}{\sqrt{\rho C_p}} \times 10^3 + n \right) \quad (25)$$

Taking the thermal parameters in these ten cases and the corresponding  $K$  values into Eq. (25), it can be solved that  $k_2 = 1.4001$ ,  $m = -0.0491$ ,  $n = 0.0109$ . So  $K$  can be expressed as:

$$K = q \times f(\lambda, \rho, C_p) = 1.4 \left( \frac{1}{\sqrt{\lambda}} - 0.05 \right) \left( \frac{1}{\sqrt{\rho C_p}} \times 10^3 + 0.01 \right) \quad (26)$$

Taking Eq. (26) and  $q = \frac{6000}{2 \times (3+4) \times 20 + 2 \times 3 \times 4} \approx 19.74$  into Eq. (21), then converting the unit of  $\tau$  from second (s) to hour (h), there is

$$T_f(\tau) = 1.18q \left( \frac{1}{\sqrt{\lambda}} - 0.05 \right) \left( \frac{1}{\sqrt{\rho C_p}} + 1 \times 10^{-5} \right) \sqrt{\tau} + \frac{q}{h} + T_0 \quad (27)$$

## (2) Applicability analysis of the new analytical method

Fig. 16 shows the air temperature changes over time though three methods for NO.1 and NO.2.

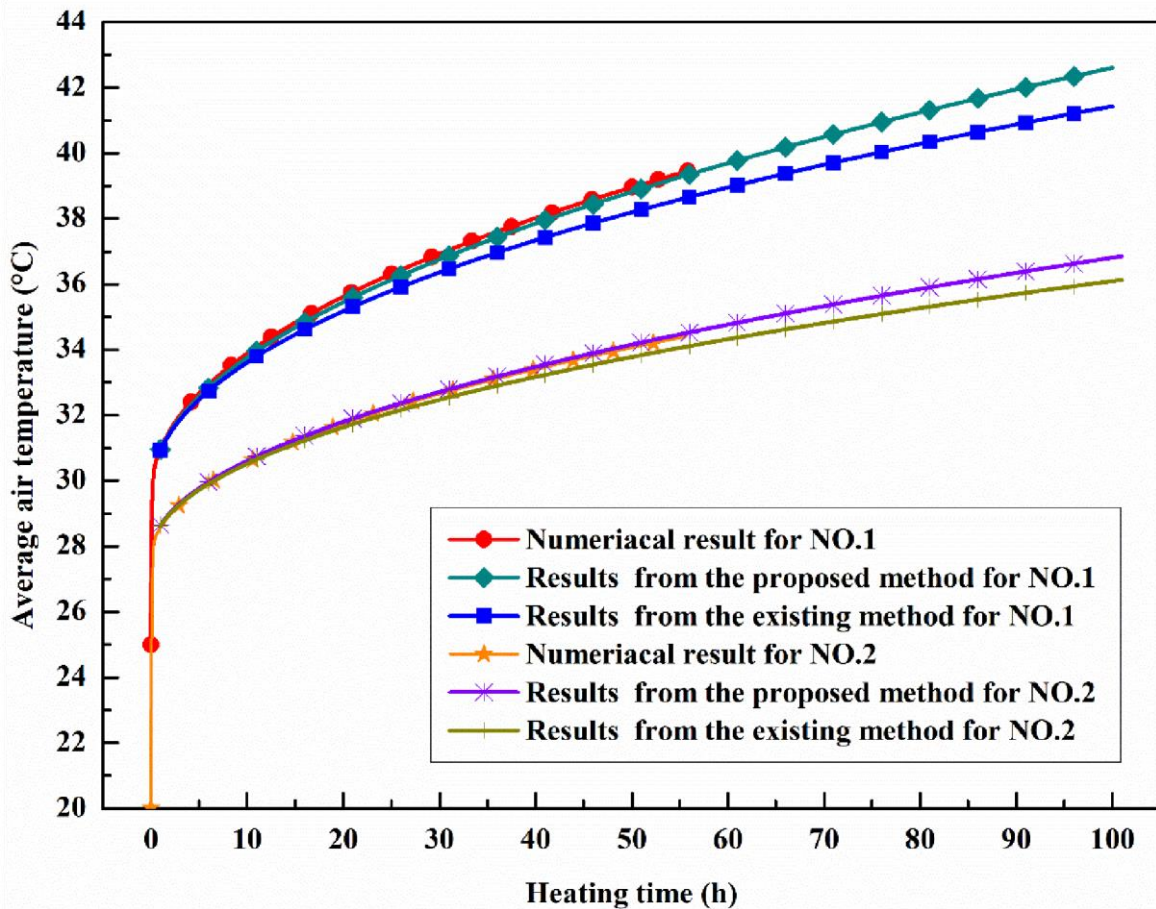


Fig. 16. Comparison of the curves obtained by three different methods for NO.1 and NO.2

It can be found in Fig. 16 that, for case NO.1 and NO.2, the air temperature calculated by Eq. (27) is closer to the numerical results than the result of Eq. (9). At 60 h, the temperature difference between the value calculated by Eq. (27) and the numerical result is less than 0.2 °C for NO.1, and less than 0.1 °C for NO.2. At 100 h, the temperature value calculated by Eq. (27) is 1.03 °C higher than the value calculated by Eq. (9) for NO.1. Taking the initial rock temperature as a reference, the difference ratio of temperature is 5.03% for NO.1 and less than 3.5% for NO.2.

Regarding the prediction of air temperature in a heated MRC under natural convection, the existing analytical method has a relatively slow temperature growth trend. The new analytical method presented in this paper are closer to numerical results than the existing methods. The difference ratio between air temperature calculated by the proposed method and the existing analytical method is less than 5% during 96 h. The proposed method is more simple and clear than the existing method in terms of expression.

## 5. Conclusions

In this study, a heating experiment is conducted and a corresponding numerical case are performed. Furtherly, another nine numerical cases with different thermal physical parameters of rock are designed to study the effect of heat conductivity, density and specific heat capacity of the rock on the thermal performance of MRC. According to the results, the following conclusions can be drawn:

(1) The experimental data and the corresponding numerical case results have similar air temperature increasing trend, which effectively validates the numerical model.

(2) The process of the air temperature increase in MRC under natural convection is divided into air temperature rapid increase stage and air temperature slow increase stage. During the previous stage, air temperature is nearly unaffected by the  $\lambda$ ,  $\rho$  and  $C_P$  of the rock. During the later stage, air temperature growth trend becomes slow with the increase of  $\lambda$ ,  $\rho$  and  $C_P$  of the rock.

(3) The surface heat transfer coefficient of the vertical wall is the largest, and it shows an obvious linear growth trend with the temperature. The predicted average natural convection heat transfer coefficient is close to a test result

(4) A new analytical calculation method for predicting the air temperature in a heated MRC under natural convection is proposed. During 96 h, the difference ratio of temperature predicted by the proposed method and the existing method is less than 5%.

The significance of the results is that it doesn't just show that, for MRC with same space volume, the trend of air temperature rising can be slowed down by increasing the surface area of the vertical walls. More importantly, through the proposed analytical method, it can be predicted in advance whether the air temperature in a MRC will exceed the allowed temperature during the 96-hour service time under natural convection, to determine whether it needs to take cooling measures in the MRC. Furthermore, it also indicates that the decoration of MRC walls by using decorative sheets with small thermal conductivity is not conducive to the heat dissipation of surrounding rocks.

## Acknowledgments

The authors would like to thank the financial support from the National Natural Science Foundation of China entitled "A study of the characteristics of the surrounding rock cold storage-phase-change heat storage coupled cooling system for mine refuge chambers" (NO. 51378426), the Youth Science and Technology Innovation Team of Sichuan Province of Building Environment and Energy Efficiency (No. 2015TD0015) and the Excellent Doctoral Thesis Cultivation Project of Southwest Jiaotong University entitled "Research on mine refuge chamber environmental

control based on pipeline compressed air” (NO. D-YB201703). The Chinese Scholarship Council is acknowledged for funding one Chinese student in space life with one-year scholarship.

## References

- [1] Q.H. Qian, P. Lin. Safety risk management of underground engineering in China: Progress, challenges and strategies. *Journal of Rock Mechanics and Geotechnical Engineering* 8 (4) (2016) 423-442.
- [2] C.D. Litton, I.E. Perera. Evaluation of criteria for the detection of fires in underground conveyor belt haulageways. *Fire Safety Journal* 51(2012) 110-119.
- [3] L.M. Yuan, L.H. Zhou, A.C. Smith. Modeling carbon monoxide spread in underground mine fires. *Applied Thermal Engineering* 100 (2016) 1319-1326.
- [4] R. Hansen, H. Ingason. Heat release rate measurements of burning mining vehicles in an underground mine. *Fire Safety Journal* 61(2013) 12-25.
- [5] M. Kobek, Z. Jankowski, z. howaniec, h. Jabłoński, Z. ąszczyk-Ożarowski. Assessment of the cause and mode of death of victims of a mass industrial accident in the Halemba coal mine. *Forensic Science International Supplement Series* 1 (1) (2009) 83-87.
- [6] C. Mejías, D. Jiménez, A. Muñoz, L. Reyes-Bozo. Clinical response of 20 people in a mining refuge: Study and analysis of functional parameters. *Safety Science* 63 (2014) 204-210.
- [7] J.L. Yang, L.W. Yang, J. Wei, Y.Z. Ma, Z.T. Zhang. Study on open-cycle carbon dioxide refrigerator for movable mine refuge chamber. *Applied Thermal Engineering* 52 (2013) 304-312.
- [8] Z.S. Xu, W.J. You, J. Kong, H.CH. Cao, C. Zhou. A study of fire smoke spreading and control in emergency rescue stations of extra-long railway tunnels. *Journal of Loss Prevention in the Process Industries Part B* 49 (2017) 155-161.
- [9] Z.J Zhang, Y.P. Yuan, K.Q. Wang. Effects of number and layout of air purification devices in mine refuge chamber. *Process Safety and Environmental Protection* 105 (2017) 338-347.
- [10] D.S. Yantek, L. Yan, P.T. Bissert, M.D. Klein. Effects of mine strata thermal behavior and mine initial temperatures on mobile refuge alternative temperature. *Mining Engineering* 69 (4) (2017) 41-48.
- [11] Z.J Zhang, Y.P. Yuan, K.Q. Wang, X.K. Gao, X.L. Cao. Experimental investigation on influencing factors of air curtain systems barrier efficiency for mine refuge chamber. *Process Safety and Environmental Protection* 102 (2016) 534-546.
- [12] E.R. Bauer, J.L. Kohler. Update on refuge alternatives: research, recommendations and underground deployment. *Mining Engineering* 61 (12 ) (2009) 51-57.
- [13] Y. Li, Y.P. Yuan, C.F. Li, X. Han, X.S. Zhang. Human responses to high air temperature, relative humidity and carbon dioxide concentration in underground refuge chamber. *Building and Environment* 131 (2018) 53-62.
- [14] Y. Du, S. Wang, L.Z. Jin, S. Wang, W.M. Gai. Experimental investigation and theoretical analysis of the human comfort prediction model in a confined living space. *Applied Thermal Engineering* 141 (2018) 61-69.
- [15] Y.X. Jia, Y.S. Liu, S.F. Sun, H.Y. Li, L.L Jiao. Refrigerating characteristics of ice storage capsule for temperature control of coal mine refuge chamber. *Applied Thermal Engineering* 75 (2015) 756-762.

- [16] S. Wang, L.Z. Jin, Z.L. Han, Y.G. Li, S.N. Ou, N. Gao, Z.L. Huang. Discharging performance of a forced-circulation ice thermal storage system for a permanent refuge chamber in an underground mine. *Applied Thermal Engineering* 110 (2017) 703-709.
- [17] X. Xu, S.J. You, X.J. Zheng, H. Zhang, S. Liu. Cooling performance of encapsulated ice plates used for the underground refuge chamber. *Applied Thermal Engineering* 112 (2017) 259-272.
- [18] Y.P. Yuan, X.K. Gao, H.W. Wu, Z.J. Zhang, X.L. Cao, L.L. Sun, N.Y. Yu. Coupled cooling method and application of latent heat thermal energy storage combined with pre-cooling of envelope: method and model development. *Energy* 119 (2017) 817-833.
- [19] X.K. Gao, Y.P. Yuan, H.W. Wu, X.L. Cao, X.D. Zhao. Coupled cooling method and application of latent heat thermal energy storage combined with pre-cooling of envelope: Optimization of pre-cooling with intermittent mode. *Sustainable Cities and Society* 38 (2018) 370-381.
- [20] X.K. Gao, Y.P. Yuan, X.L. Cao, H.W. Wu, X.D. Zhao. Coupled cooling method and application of latent heat thermal energy storage combined with pre-cooling of envelope: Sensitivity analysis and optimization. *Process Safety and Environmental Protection* 107 (2017) 438-453.
- [21] X.K. Gao, Z.J. Zhang, Y.P. Yuan, X.L. Cao, C. Zeng, D. Yan. Coupled cooling method for multiple latent heat thermal storage devices combined with pre-cooling of envelope: Model development and operation optimization. *Energy* 159 (2018) 508-524.
- [22] Y.P. Yuan, B.Y. Cheng, J.F. Mao, Y.X. Du. Effect of the thermal conductivity of building materials on the steady-state thermal behavior of underground building envelopes. *Building and Environment* 41 (3) (2006) 330-335.
- [23] Y.P. Yuan, H.H. Ji, Y.X. Du, B.Y. Cheng. Semi-analytical solution for steady-periodic heat transfer of attached underground engineering envelope. *Building and Environment* 43 (6) (2008) 1147-1152
- [24] Y.M. Xiao, X.C. Liu, R.R. Zhang. Calculation of transient heat transfer through the envelope of an underground cavern using Z-transfer coefficient method. *Energy and Buildings* 48 (2012) 190-198
- [25] X.C. Liu, Y.M. Xiao, K. Inthavong, J.Y. Tu. A fast and simple numerical model for a deeply buried underground tunnel in heating and cooling applications. *Applied Thermal Engineering* 62 (2) (2014) 545-552.
- [26] L. Kajtar, J. Nyers, J. Szabo. Dynamic thermal dimensioning of underground spaces. *Energy* 87 (2015) 361-368.
- [27] J. Szabó, L. Kajtár, J. Nyers, B. Bokor. A new approach and results of wall and air temperature dynamic analysis in underground spaces. *Energy* 106 (2016) 520-527.
- [28] A.P. Sasmito, J.C. Kurnia, E. Birgersson, A.S. Mujumdar. Computational evaluation of thermal management strategies in an underground mine. *Applied Thermal Engineering* 90 (2015) 1144-1150.
- [29] A. Habibi, R.B. Kramer, A.D.S. Gillies. Investigating the effects of heat changes in an underground mine. *Applied Thermal Engineering* 90 (2015) 1164-1171.
- [30] A.G. Li, C.Q. Yang, T. Ren. Modeling and parametric studies for convective heat transfer in large, long and rough circular cross-sectional underground tunnels. *Energy and Buildings* 127 (2016) 259-267.
- [31] Y. Du, W.M. Gai, L.Z. Jin, S. Wang. Thermal comfort model analysis and optimization performance evaluation of a multifunctional ice storage air conditioning system in a confined mine refuge chamber. *Energy* 141 (2017) 964-974.

- [32] A.D.S. Gillies, P.G. Creevy, G. Danko, et al. Determination of the in situ mine surface heat transfer coefficient. Proceedings, Fifth U S Mine Ventilation Symposium, Society of Mining Engineers 1991:288-298.
- [33] F.Q. Huang, J.Y. Zhang, S.M. Xie, A.X. Wang. The Thermal Calculation Method of Underground Engineering [M] China Architecture and Building Press, Beijing 1983 (in Chinese).
- [34] S.M. Yang, W.Q. Tao. Heat transfer. Higher Education press, Beijing, 2006 (in Chinese).
- [35] X.J. Meng, Y. Wang, T.N. Liu, X. Xing, Y.X. Cao, J.P. Zhao. Influence of radiation on predictive accuracy in numerical simulations of the thermal environment in industrial buildings with buoyancy-driven natural ventilation. Applied Thermal Engineering 96 (2016) 473–480.
- [36] T. Wu, C.W. Lei. On numerical modelling of conjugate turbulent natural convection and radiation in a differentially heated cavity. International Journal of Heat and Mass Transfer. 91 (2015) 454-466.
- [37] J. Franke, C. Hirsch, A.G. Jensen, H.W. Krüs, M. Schatzmann, et al. Recommendations on the use of CFD in wind engineering. Proceedings of the International Conference on Urban Wind Engineering and Building Aerodynamics, Belgium, 5–7 May 2004.
- [38] D.N. Sørensen, P.V. Nielsen. Quality control of computational fluid dynamics in indoor environments. Indoor Air, 13 (2003), 2-17.
- [39] E. Bacharoudis, M.G. Vrachopoulos, M.K. Koukou, D. Margaris, A.E. Filios, S.A. Mavrommatis. Study of the natural convection phenomena inside a wall solar chimney with one wall adiabatic and one wall under a heat flux. Applied Thermal Engineering 27 (2007) 2266–2275.
- [40] A. Piña-Ortiz, J.F. Hinojosa, V.M. Maytorena. Test of turbulence models for natural convection in an open cubic tilted cavity. International Communications in Heat and Mass Transfer 57 (2014) 264–273.
- [41] A. Piña-Ortiz, J.F. Hinojosa, J. P. Xamán, V.M. Maytorena. Test of turbulence models for heat transfer within a ventilated cavity with and without an internal heat source. International Communications in Heat and Mass Transfer 94 (2018) 106–114.
- [42] M. Boulet, B. Marcos, M. Dostie, C. Moresoli. CFD modeling of heat transfer and flow field in a bakery pilot oven. Journal of Food Engineering 97 (2010) 393–402.
- [43] C. Yoon, S. Kwon, J. Kim, H. Choi. An experimental study regarding the determination of seasonal heat transfer coefficient in KURT by convection conditions. Safety Science 51 (2013) 241-249.